





22 highly correlated with the observation results. Our study confirms the correctness of the qualitative  
23 description of the relationship between AEP and  $P_{df}$ , clarifies that debris flow is a small probability  
24 event compared to rainfall frequency, and quantitatively reveals the evolution law of debris flow  
25 occurrence probability with AEP, which can provide a clear reference for the early warning of debris  
26 flows.

27 **Keywords:** Debris flow, antecedent effective rainfall, Dens-ID, Monte Carlo method

28

## 29 **1 Introduction**

30 The antecedent effective precipitation (AEP) is similar to a Trojan horse lurking inside a loose  
31 soil mass, which can cooperate with subsequent rainfall at any time to trigger debris flow in a gully.  
32 The AEP is equivalent to the preservation of precipitation in the soil mass before the triggering  
33 rainfall process; it represents the saturation degree of the loose soil mass (Segoni et al., 2018a;  
34 Leonarduzzi and Molnar, 2020). Therefore, the soil moisture that has accumulated from antecedent  
35 rainfall since the beginning of a rainfall season has a significant influence on how new storm rainfall  
36 interacts with the loose soil mass within a gully (Fiorillo and Wilson, 2004; Long et al., 2020). If a  
37 loose solid material is provided by shallow landslides or channel erosion, its shear strength is  
38 decreased by an increase in AEP (Papa, et al., 2013; Senthilkumar et al., 2017; Liu et al., 2020), and  
39 in the subsequent rainfall process, the supply rate of solid material resources can be significantly  
40 enhanced (Wei et al., 2008; Bennett et al., 2014; Zhang et al., 2020). Additionally, increased AEP  
41 and moisture content have been shown to enhance surface rainfall-induced runoff in a variety of  
42 environments (Tisdall, 1951; Luk, 1985; Le Bissonnais et al., 1995; Castillo et al., 2003; Jones et  
43 al., 2017; Hirschberg et al., 2021). Thus, AEP plays an important role in the formation of debris



44 flows (Hong et al., 2018).

45       The rainfall threshold represents the degree of difficulty of debris flow triggered by rainfall  
46 (Marra et al., 2017). Investigations, such as the influence of AEP on the rainfall threshold, can be  
47 helpful in examining the relationship between AEP and debris flow occurrence. Currently,  
48 conclusions drawn from the analysis of the relationship between the AEP and rainfall threshold are  
49 relatively consistent, and there is a negative correlation between the AEP and rainfall conditions  
50 (such as daily rainfall) that trigger debris flows (Huang, 2013). AEP represents the degree of  
51 saturation of the loose soil mass (Zhao et al., 2019a; Abraham et al., 2021), and integrating soil  
52 moisture with rainfall thresholds has been proven effective in improving these thresholds (Segoni  
53 et al., 2018a; Zhao et al., 2019b; Abraham et al., 2020), as the antecedent moisture content plays a  
54 key role in the soil shear strength. Scholars have attempted to analyze the influence of antecedent  
55 soil moisture on the rainfall threshold triggering debris flow (Cui et al., 2007; Hu et al., 2015).  
56 Similar to the relationship between AEP and rainfall threshold, there is a negative correlation  
57 between antecedent soil moisture and triggering rainfall conditions (Chen et al., 2017). The above  
58 investigations on the AEP and antecedent soil moisture show that the AEP can significantly decrease  
59 the rainfall conditions that trigger a debris flow, which in turn means that debris flow is more likely  
60 to occur. Therefore, there is the following consensus in the field of debris flow: the greater the AEP,  
61 the higher the probability ( $P_{df}$ ) of subsequent rainfall triggering the debris flow (De Vita et al., 2000;  
62 Bel et al., 2017). Therefore, discovering a specific function to describe this qualitative description  
63 is helpful in further demonstrating the above consensus, revealing a certain evolutionary law of  
64 debris flow with rainfall in nature. Long-term observational data may be used to achieve this purpose;  
65 however, the number of debris flow gullies with long-term observational data worldwide is less than



66 10 (Hürlimann et al., 2019). Even at a field site, such as Jiangjia Gully, it has been difficult to provide  
67 sufficient observational data to accomplish this goal for more than 60 years.

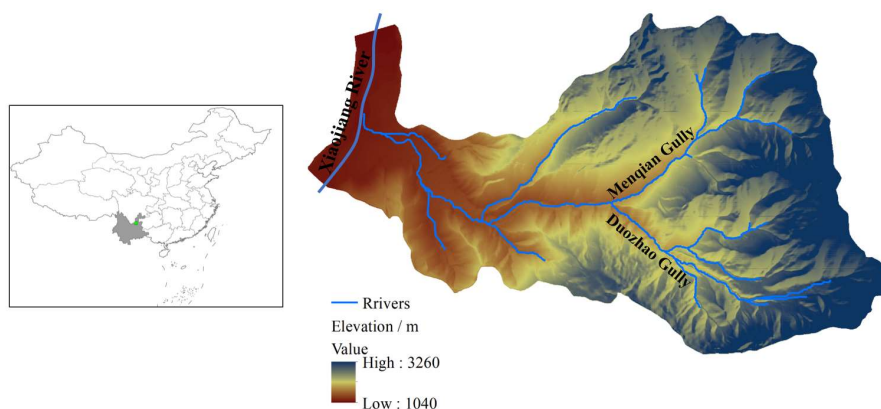
68 To quantify the evolution law of  $P_{df}$  with AEP variation, a numerical model that can correlate  
69 the rainfall parameters (I and D) with the debris flow density (Zhang et al., 2020; Long et al., 2020)  
70 was denoted as the Dens-ID model and was used to construct the rainfall intensity-duration (ID)  
71 threshold curve database for different AEP. The ID threshold curves with upper and lower bounds  
72 can delineate the closed region in the ID coordinate system, which represents the set of all rainfall  
73 conditions that can trigger debris flow at a certain AEP. Consequently, the probability of natural  
74 rainfall falling into a closed region is equivalent to  $P_{df}$ , which can then be calculated based on Monte  
75 Carlo integration. The next section introduces the basic information of study area including the  
76 rainfall and debris flow event data collected from the study area. The third section addresses how to  
77 establish the functional relationship between the AEP and  $P_{df}$  using the Dens-ID and Monte Carlo  
78 integration method. Section 4 and 5 discuss the results and state the conclusions of this study,  
79 respectively.

## 80 **2 Study area**

81 The Jiangjia Gully (JJG), a primary tributary of the Xiaojiang River, is located in the  
82 Dongchuan District of Kunming City, Yunnan Province, China (Fig.1). As shown in Fig.1, JJG has  
83 a drainage area of 48.6 km<sup>2</sup> with elevations ranging from 1040–3260 m. In this gully, the relative  
84 relief from the ridge to the valley reaches 500 m, and most of the slope gradient is greater than 25°.  
85 Slopes within JJG are covered by abundant loose soil with a thickness of more than ten meters.  
86 Shallow landslides are frequently triggered by intense rainfall processes in JJG, providing a large  
87 amount of solid materials for debris flow (Yang et al., 2022). The Menqian and Duo Zhao gullies,



88 shown in Fig.1, are the two main tributaries of JJG, accounting for 64.7% of the entire drainage area.  
89 The upstream areas of the two main tributaries are the initiation zones of the debris flows, and the  
90 channels of the upstream tributaries are narrow and V-shaped (Zhang et al., 2020).



91

92

Fig.1 Location of JJG

93 Steep terrain provides a beneficial potential energy condition for transporting a large amount  
94 of loose solid materials from JJG to Xiaojiang River. Consequently, debris flows in JJG can be easily  
95 triggered by rainfall. Based on the collected rainfall data, high-intensity rainstorm or long-duration  
96 rainfall processes can cause debris flow occurrence (Zhang et al., 2020). The solid material  
97 necessary for a debris flow in a gully may be sourced from shallow landslides (Iverson et al., 1997;  
98 Gabet and Mudd, 2006; Zhang et al., 2020; Long et al., 2020) or runoff-induced bed erosions (Berti  
99 and Simoni, 2005; Coe et al., 2008; Tang et al., 2020; Bernard and Gregoretti, 2021). In JJG, the  
100 solid material is sourced primarily from shallow landslides (Zhang et al., 2014; Liu et al., 2016;  
101 Yang et al., 2022), which is consistent with the assumptions of Dens-ID (Zhang et al., 2020). Thus,  
102 JJG is used as the study zone for deriving the function that describes the relationship between AEP  
103 and  $P_{df}$ .

104 The JJG datasets for Dens-ID are terrain data, hydrological parameters, and soil mechanical



105 parameters. The DEM is the basal data for deriving other terrain data, including slope length,  
106 gradient, and river channels; the spatial resolution of the DEM is 0.5 m, and a DEM with a grid size  
107 of 10 m was generated using the resampling technology in ArcGIS. The hydrological parameters  
108 are related to the soil types within JJG; the five key parameters are the saturated soil water content,  
109 residual soil water content, the two parameters of soil water characteristic curve including  $n$  and  $m$ ,  
110 and the infiltration rate of topsoil. The soil mechanical parameters are the soil cohesion force and  
111 internal friction angle, which were obtained through direct shear tests on the soil samples. Detailed  
112 data are available in Zhang et al. (2020) and Long et al. (2020).

113 Rainfall data for the rainy seasons between 2006 and 2020 were collected from the JJG  
114 observation station, and it was necessary to identify each rainfall process from the long-term rainfall  
115 sequences. Inter-event time (IET) was defined as the minimum time interval between two  
116 consecutive rainfall pulses (Adams et al., 1986). IET has a strong influence on the rainfall event  
117 starting and ending times (Bel et al., 2017), and Peres et al. (2018) identified that IET depends on  
118 whether the mean daily potential evapotranspiration (MDPE) is larger than precipitation within the  
119 IET. The long observation of evaporation within JJG showed that MDPE is about 4 mm;  
120 precipitation during IET > 0.5 mm is considered the end of a rainfall process. Under this standard,  
121 1094 rainfall events and 37 debris flow events were identified during the sampling period. Detailed  
122 rainfall data information can be found in “appendix 1-1094 rainfall and 37 debris flow data.xlsx”.  
123 The AEP listed in this appendix was considered the weighted sum of the rainfall periods before the  
124 occurrence of debris flow (Long et al., 2020) and it can be calculated using Eq. 1.

125

$$AEP = \sum_{i=1}^n K^n R_i \quad (1)$$



126 where AEP is the antecedent effective rainfall;  $K$  is the attenuation coefficient, which is equal to  
127 0.78 based on the field test in JJG (Zhang et al., 2020); and  $n$  is the number of days preceding the  
128 debris flow occurrence.

129 Based on the observed rainfall data, the 1094 AEPs were calculated using Eq. 1 and are listed  
130 in Appendix 1. The AEP corresponding to each rainfall event varies from 0–88 mm. Taking this  
131 variation range as a reference, the variation range of the AEP input in the Dens-ID model was set  
132 between 10 and 130 mm. When the AEP was less than 90 mm, it was gradually increased by 5 mm;  
133 after the AEP was larger than 90 mm, its increment was set to 10 mm. Dens-ID presets several AEP  
134 values including 10, 15, 20, 25, 30, 35, 40, 45, 50, 55, 60, 65, 70, 75, 80, 85, 90, 100, 110, 120, and  
135 130 mm.  $P_{df}$  can be calculated under different AEP conditions. The preset AEP values exceeded the  
136 observed maximum value of 88 mm because we wanted to observe whether  $P_{df}$  tended to stabilize  
137 and determine its boundary value

### 138 3 Methods

#### 139 3.1 Dens-ID

140 Debris flow gullies, characterized by a solid source supply from landslides, are widely  
141 distributed in southwest China (Zhang et al., 2014). For this type of debris flow gully, our previous  
142 study proposed a numerical model (denoted as Dens-ID) based on the evolution law of fluid density  
143 (Zhang et al., 2020; Long et al., 2020). Den-ID assumes the debris flow to be a water-soil mixture.  
144 Based on the digital elevation model (DEM) of a gully, Den-ID, which uses a grid cell as a basic  
145 mapping unit, can simulate the surface runoff and water diffusion in the vertical direction within the  
146 soil mass.

$$147 \quad -D(\theta) \frac{\partial \theta}{\partial z} + K(\theta) = I(t) \quad (2)$$



148 where  $\theta$  is the soil water content;  $D(\theta) = K(\theta)/(d\theta/d\psi)$ , which represents the soil water  
149 diffusivity;  $z$  is the soil depth, which is positive downwards along the soil depth as the topsoil is  
150 taken as the origin point;  $K(\theta)$  is the hydraulic conductivity;  $I(t)$  is the rainfall intensity; and  $\psi$  is  
151 the soil matrix suction. When the rainfall intensity was less than the surface infiltration capacity, Eq.  
152 2 was used to represent this physical process. The case of precipitation intensity exceeding the  
153 infiltration capacity of topsoil means that the surface is saturated, and the excess precipitation from  
154 the topsoil is typically converted into runoff; therefore, the pressure infiltration of each grid cell is  
155 not considered. As the topsoil is saturated by rainfall, Eq. 2, which controls the infiltration border,  
156 uses  $\theta = \theta_s$ , where  $\theta_s$  is the saturated water content of a soil type within a debris flow gully.

$$157 \quad \frac{\partial \theta}{\partial t} = \frac{\partial}{\partial z} \left[ D(\theta) \frac{\partial \theta}{\partial z} \right] - \frac{\partial K(\theta)}{\partial \theta} \quad (3)$$

158 Eq. 3 is the Richard differential infiltration equation (Richards, 1931), which is used to describe the  
159 water movement law along the vertical direction within the soil mass after precipitation infiltrates  
160 the topsoil. Dens-ID uses the finite-difference method to solve Eqs. 2 and 3 and can provide the  
161 runoff depth (denoted as  $dw(i, t)$ ), soil water content, and soil matrix suction for each grid cell.  
162 Dens-ID then calculates the runoff volume using runoff depth  $dw(i, t)$  in Eq. 4.

$$163 \quad V_w(t) = \sum_{t=1}^T \sum_{i=1}^n S_g * dw(i, t) \quad (4)$$

164 where  $n$  represents the total number of grid cells that can generate runoff at time  $t$  and  $V_w(t)$   
165 represents the total volume of runoff within a gully at time  $t$ .

166 Taking hydrological parameters such as soil water content and soil matrix suction as inputs,  
167 Dens-ID uses Eqs. 5 and 6 to estimate the supply volume of rainfall-induced loose solid materials  
168 within a gully. Eq. 5 calculates safety factor  $F_s$  of each grid cell as a function of the matrix suction  
169 and soil moisture.  $F_s > 1$  indicates that the grid cell is stable and cannot supply solid material to the





170 gully, whereas a grid with  $F_s < 1$  can provide solid material in the form of a shallow landslide.

$$171 \quad F_s = \frac{\tan \varphi}{\tan \beta} + \frac{c + \psi \tan(\varphi^b)}{\gamma_t d_s \cos \beta \sin \beta} \quad (5)$$

172 where  $F_s$  represents the safety factor of each grid cell,  $c$  is the soil cohesion force,  $\varphi$  is the internal  
173 friction angle,  $\varphi^b$  is related to the matrix suction and is approximately equal to  $\varphi$  as the low matrix  
174 suction is small,  $d_s$  is the soil depth, and  $\psi$  is the matrix suction of the soil, a function of soil water  
175 content, and can be described by the Van Genuchten model (Van Genuchten, 1980).

176 Using  $d_s$  derived from Eq. 5 as input, Eq. 6 is used to estimate the total volume of solid  
177 materials provided from all the instable grid cells in the gully from the beginning to the end of the  
178 rainfall process.

$$179 \quad V_s(t) = \sum_{t=1}^T \sum_{j=1}^m S_g * ds(j, t) \quad (6)$$

180 where  $m$  represents the number of grid cells that can provide solid material at time  $t$  and  $V_s(t)$  is the  
181 total volume of solid material within a gully at time  $t$ . At time  $t$ , the density of the water-soil mixture  
182 after full coupling between runoff and solid material can be calculated using Eq. 7.

$$183 \quad \rho_{mix}(t) = \frac{\rho_w V_w(t) + \rho_s V_s(t)}{V_{mix}(t)} \quad (7)$$

184 where  $\rho_{mix}(t)$  is the density of the water-soil mixture,  $\rho_w$  is the water density,  $\rho_s$  is the density of  
185 the soil particles, and  $V_{mix}(t)$  is the volume of the water-soil mixture, which is the sum of  $V_w(t)$   
186 and  $V_s(t)$ .  $V_w(t)$  and  $V_s(t)$  are the key variables that can be derived using Eqs. 4 and 6.

187 Dens-ID presets the density of the water-soil mixture as  $\rho_{mix}$ . By simulating many rainfall  
188 scenarios, including long durations with low-intensity rainfall and short durations with high-  
189 intensity rainfall, Dens-ID can obtain adequate combinations of  $[D_i, I_i]$ . Using each  $[D_i, I_i]$  as input,  
190 Dens-ID derives the density value via hydrology simulation and estimate the solid material and  
191 runoff volumes. When the calculated density is equal to  $\rho_{mix}$ , the  $[D_i, I_i]$  combination is saved by



192 Dens-ID. After Dens-ID completes the trial calculations, all combination data of  $[D_i, I_i]$  that satisfy  
193 the constraints of the preset density ( $\rho_{\text{mix}}$ ) can be collected, forming a dataset. Each collected  $[D_i, I_i]$   
194 within the dataset corresponds to  $\rho_{\text{mix}}$ ; therefore, Dens-ID can map rainfall parameters (D and I) and  
195 debris flow density (Long et al., 2020). Dens-ID can derive the ID threshold curves by fitting the  
196 selected  $[D_i, I_i]$  data; each ID curve corresponds to a debris flow density value (Zhang et al., 2020).  
197 As the density of debris flow in JJG varies in a specific interval of  $1.2\text{--}2.3\text{g/cm}^3$  (Zhang et al., 2014;  
198 Zhuang et al., 2015; Long et al., 2020), the threshold curve that corresponds to the boundary value  
199 can form a closed area with the I- and D-axes in the ID coordinate system. The case of monitoring  
200 or forecasting rainfall falling into this closed area in the I-D coordinate system indicates that the  
201 rainfall condition may trigger debris flow. The verification results for JJG show that Dens-ID  
202 effectively describes the mechanism and process of debris flow formation using shallow landslides  
203 as a solid source supply, and its prediction accuracy is approximately 80.5%, which is 27.7% higher  
204 than that of statistical models (Zhang et al., 2020). Such a high prediction accuracy can further  
205 indicate that the closed area formed by the derived ID curves has a very reasonable location and  
206 coverage in the ID coordinate system, providing extremely reliable analytical data in this study.

207 .

### 208 3.2 Monte Carlo method for calculating the definite integral

209 Because of the boundary of the debris-flow density in JJG ( $1.2\text{--}2.3\text{g/cm}^3$ ), Dens-ID produces  
210 the corresponding upper and lower boundary curves under a specific AEP condition. The two  
211 boundary curves can be described using the power function

$$212 \begin{cases} f(D)_{up} = I_{up} = \alpha_1 D^{\beta_1} & D \in [a_1, b_1] \\ f(D)_{low} = I_{low} = \alpha_2 D^{\beta_2} & D \in [a_2, b_2] \end{cases} \quad (8)$$



213           These two threshold curves can form a closed warning area in the ID coordinate system,  
214   denoted as  $W_{ID}$ . The independent variable (D) and dependent variable (I) in Eq. 8 also form a closed  
215   rectangular region in the ID coordinate system, denoted as  $R_{ID}$ . In the ID coordinate system, the  
216   coverage of  $R_{ID}$  is larger than that of  $W_{ID}$ , as will be shown in detail in Section 4.1. Within  $R_{ID}$ , if  
217   certain rainfall processes are located in  $W_{ID}$ , this rainfall condition can trigger debris flow. As long  
218   as the probability of rainfall falling into the range of  $W_{ID}$  under random conditions can be  
219   determined, the occurrence probability of debris flow can be estimated for a specific AEP. Many  
220   physical phenomena are stochastic in nature and governed by stochastic partial differential equations  
221   with nondeterministic initial/boundary conditions or integral equations (Yan and Hong, 2014).  
222   Albert (1956) proposed the Monte Carlo method for solving integral equations. This method was  
223   subsequently used to estimate the peak flow and volume of debris flow (Donovan and Santi, 2017;  
224   Paola et al., 2017), entrainment of the underlying bed sediment (Han et al., 2015), and risk  
225   assessment (Calvo and Savi, 2009; Li et al., 2021). Based on the Monte Carlo principle (Peres and  
226   Cancelliere, 2014), the probability of the rainfall condition within the  $R_{ID}$  range falling into the  $W_{ID}$   
227   range can be determined using  $W_{ID}/R_{ID}$ . The physical meaning of the Monte Carlo solving definite  
228   integral is the estimation of the area enclosed by the function curve and horizontal axis. Therefore,  
229   the area of  $W_{ID}$  can be calculated by the difference in the definite integral formula of the two  
230   equations in Eq. 7.

$$231 \quad W_{ID} = S_{up} - S_{low} = \int_{a_1}^{b_1} f(D)_{up} dD - \int_{a_2}^{b_2} f(D)_{low} dD \quad (9)$$

232   where  $S_{up}$  and  $S_{low}$  represent the area enclosed by the two threshold curves and the horizontal axis,  
233   respectively, and  $a_1$ ,  $b_1$ ,  $a_2$ , and  $b_2$  are the boundary values of D in the two curves. For the upper  
234   boundary line (or lower boundary), if the probability distribution function of D between  $[a_1, b_1]$  is



235  $p(D)$ , Eq. 9 can be derived by substituting  $p(D)$  into Eq. 8, which is used to calculate  $S_{up}$  and  $S_{low}$ .

$$236 \quad \begin{cases} S_{up} = \int_{a_1}^{b_1} f(D)_{up} dD = \int_{a_1}^{b_1} \frac{f(D)_{up}}{p(D)} p(D) dD \approx \frac{1}{n} \sum_{k=1}^n \frac{f(D_i)_{up}}{p(D_i)} \\ S_{low} = \int_{a_2}^{b_2} f(D)_{low} dD = \int_{a_2}^{b_2} \frac{f(D)_{low}}{p(D)} p(D) dD \approx \frac{1}{n} \sum_{k=1}^n \frac{f(D_i)_{low}}{p(D_i)} \end{cases} \quad (10)$$

$$237 \quad W_{ID} = \frac{1}{n} \sum_{k=1}^n \frac{f(D_i)_{up}}{p(D_i)} - \frac{1}{n} \sum_{k=1}^n \frac{f(D_i)_{low}}{p(D_i)} \quad (11)$$

238 where  $n$  represents the number of random samples drawn from the variation range of  $D$  and  $p(D_i)$   
 239 is the probability density distribution function of  $D$  in the interval  $[a_1, b_1]$  or  $[a_2, b_2]$ . The key to  
 240 solving Eq. 10 is sampling from  $p(D)$ . The following steps were used to explain how samples were  
 241 taken using  $p(D_i)$ .

242 Step 1: Based on the probability density distribution function  $p(D)$ , the cumulative probability  
 243 distribution function can be derived by  $cdf(D) = \int_{-\infty}^D f(D) dD$ ;

244 Step 2: Assume that  $U^{(i)}$  obeys a uniform distribution within  $[0, 1]$ , which can be randomly collected  
 245 from this interval and denoted as  $U^{(i)} \sim U(0, 1)$ .

246 Step 3: Substitute  $U^{(i)}$  into the inverse function of the cumulative probability distribution  $cdf(D)$  to  
 247 obtain random sample  $D^{(i)}$ , denoted by  $D^{(i)} = cdf^{-1}(U^{(i)})$ . Then, a dataset composed of  $n$  data  
 248 points of  $D^{(i)}$  was obtained.

249 Step 4:  $W_{ID}$  can be calculated by substituting  $n$  data points of  $D^{(i)}$  into Eq. 10, and the  $P_{df}$  ( $P_{df} =$   
 250  $\frac{R_{ID}}{W_{ID}}$ ) corresponding to a specific AEP is determined.  $P_{df}$  represents the probability that the  
 251 subsequent precipitation process may trigger debris flow for a certain AEP. Thus, the influence of  
 252 the AEP on the occurrence probability of debris flows can be quantified.

### 253 3.3 Correlation analysis between numerical and observation results

254 The relationship between the AEP- $P_{df}$  fit through the observational data was used as a reference  
 255 standard, and the correlation analysis method was used to verify the function of the AEP- $P_{df}$  derived



256 by Dens-ID. Correlation analysis was used to study the degree of linear correlation between  
 257 variables, which is represented by correlation coefficient  $r$ :

$$258 \quad r = \frac{\sum_{i=1}^n (x_i - \bar{x})(y_i - \bar{y})}{\sqrt{\sum_{i=1}^n (x_i - \bar{x})^2 \sum_{i=1}^n (y_i - \bar{y})^2}} \quad (12)$$

259 where  $x$  represents the  $P_{df}$  derived from the observed data,  $y$  represents the  $P_{df}$  derived from Dens-  
 260 ID,  $\bar{x}$  and  $\bar{y}$  represent the averages,  $r$  represents the correlation coefficient, and  $n$  represents the  
 261 number of samples.  $|r| \geq 0.8$  can be regarded as a high correlation between two variables;  $0.5 \leq |r| < 0.8$   
 262 represents a moderate correlation;  $0.3 \leq |r| < 0.5$  represents a low correlation; and  $|r| < 0.3$  indicates the  
 263 degree of correlation between the two variables is weak and can be regarded as uncorrelated.

## 264 4 Results and discussion

### 265 4.1 ID threshold curves and warning zone closed by the derived curves

266 The ID threshold curves corresponding to the different AEPs derived from Dens-ID are listed  
 267 in Table 1. Each AEP corresponded to the upper and lower boundary lines of the ID threshold, and  
 268 these two boundary lines corresponded to different debris flow density values. In Table 1, when  
 269  $AEP \leq 15$  mm, the maximum density corresponding to the ID threshold curve cannot reach 2.2, which  
 270 are equal to 1.8 and 2.0 when  $AEP = 10$  and 15 mm. This is because a lower AEP makes the supply  
 271 rate of solid resources in JGG far less than the runoff rate during rainfall (Long et al., 2020). At this  
 272 time, Dens-ID determines that it is easier to form a low-density water-soil mixture in JGG.

273 Table 1 ID threshold curve database under different AEP

AEP (mm)	ID threshold curve function for JGG	
	1.2 g/cm <sup>3</sup>	2.2 g/cm <sup>3</sup>
10	$I_{1.2} = 19.85D^{-0.54} D \in [1, 269] (R^2 = 0.991)$	$I_{1.8} = 15.85D^{-0.48} D \in [1, 263] (R^2 = 0.990)$
15	$I_{1.2} = 21.69D^{-0.55} D \in [1, 236] (R^2 = 0.993)$	$I_{2.0} = 16.10D^{-0.50} D \in [1, 229] (R^2 = 0.995)$
20	$I_{1.2} = 23.22D^{-0.58} D \in [1, 203] (R^2 = 0.996)$	$I_{2.2} = 17.20D^{-0.53} D \in [1, 192] (R^2 = 0.995)$
25	$I_{1.2} = 24.47D^{-0.60} D \in [1, 171] (R^2 = 0.997)$	$I_{2.2} = 16.92D^{-0.53} D \in [1, 160] (R^2 = 0.998)$

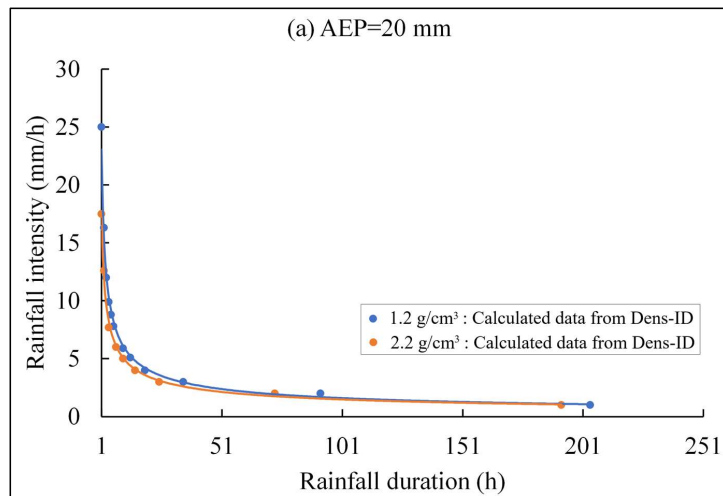


30	$I_{1,2}=26.24D^{-0.64} D \in [1, 143] (R^2=0.996)$	$I_{2,2}= 18.09D^{-0.57} D \in [1, 132] (R^2=0.995)$
35	$I_{1,2}=35.47D^{-0.65} D \in [1, 123] (R^2=0.958)$	$I_{2,2}= 19.55D^{-0.58} D \in [1, 112] (R^2=0.985)$
40	$I_{1,2}= 40.59D^{-0.78} D \in [1, 103] (R^2=0.966)$	$I_{2,2}= 22.15D^{-0.64} D \in [1, 92] (R^2=0.984)$
45	$I_{1,2}= 41.12D^{-0.78} D \in [1, 83] (R^2=0.932)$	$I_{2,2}= 23.19D^{-0.69} D \in [1, 72] (R^2=0.981)$
50	$I_{1,2}=41.26D^{-0.86} D \in [1, 65] (R^2=0.981)$	$I_{2,2}= 23.50D^{-0.74} D \in [1, 55] (R^2=0.980)$
55	$I_{1,2}=38.63D^{-0.88} D \in [1, 53] (R^2=0.950)$	$I_{2,2}= 23.31D^{-0.70} D \in [1, 42] (R^2=0.932)$
60	$I_{1,2}= 31.49D^{-0.92} D \in [1, 40] (R^2=0.992)$	$I_{2,2}= 20.73D^{-0.86} D \in [1, 30] (R^2=0.977)$
65	$I_{1,2}= 29.14D^{-0.95} D \in [1, 32] (R^2=0.957)$	$I_{2,2}= 18.10D^{-0.91} D \in [1, 22] (R^2=0.893)$
70	$I_{1,2}= 23.05D^{-0.96} D \in [1, 25] (R^2=0.998)$	$I_{2,2}= 13.04D^{-0.93} D \in [1, 15] (R^2=0.995)$
75	$I_{1,2}= 21.13D^{-0.97} D \in [1, 22] (R^2=0.994)$	$I_{2,2}=10.90D^{-0.95} D \in [1, 12] (R^2=0.995)$
80	$I_{1,2}= 18.72D^{-0.98} D \in [1, 20] (R^2=0.997)$	$I_{2,2}= 9.96D^{-0.95} D \in [1, 11] (R^2=0.999)$
85	$I_{1,2}= 18.47D^{-0.99} D \in [1, 18] (R^2=0.999)$	$I_{2,2}= 8.17D^{-0.95} D \in [1, 9] (R^2=0.999)$
90	$I_{1,2}= 16.99D^{-0.98} D \in [1, 18] (R^2=0.999)$	$I_{2,2}=6.81D^{-0.95} D \in [1, 7] (R^2=0.994)$
100	$I_{1,2}= 16.90D^{-0.98} D \in [1, 18] (R^2=0.999)$	$I_{2,2}=6.81D^{-0.95} D \in [1, 7] (R^2=0.994)$
110	$I_{1,2}= 16.87D^{-0.98} D \in [1, 16] (R^2=0.999)$	$I_{2,2}=6.76D^{-0.95} D \in [1, 7] (R^2=0.997)$
120	$I_{1,2}= 16.87D^{-0.98} D \in [1, 16] (R^2=0.999)$	$I_{2,2}=6.76D^{-0.95} D \in [1, 7] (R^2=0.997)$
130	$I_{1,2}= 16.87D^{-0.98} D \in [1, 16] (R^2=0.999)$	$I_{2,2}=6.76D^{-0.95} D \in [1, 7] (R^2=0.997)$

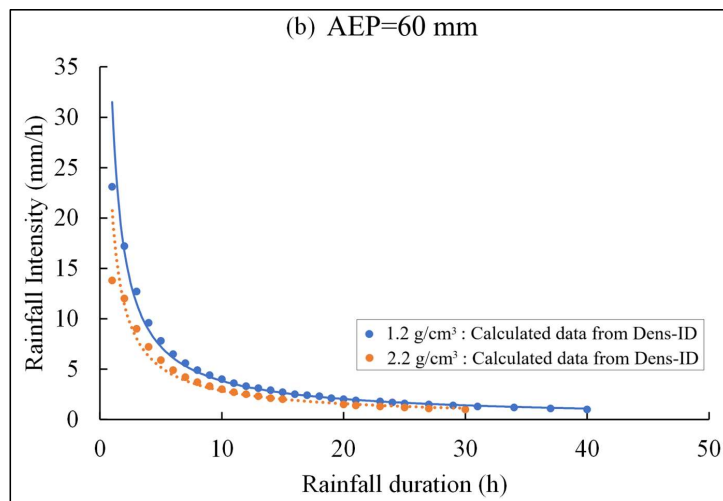
274 When AEP < 10 mm, Dens-ID cannot derive the threshold curve corresponding to even the  
 275 minimum density value of 1.2 g/cm<sup>3</sup>, which indicates that the subsequent rainfall can hardly trigger  
 276 debris flow JIG. Table 1 also shows that when the AEP reaches 110 mm,  $\alpha$  and  $\beta$  in the threshold  
 277 curve become constant and no longer change with AEP. An AEP ranging from 10 to 110 mm can  
 278 affect the debris flow formation in JIG. After the AEP in Table 1 exceeded 90 mm, the effect of AEP  
 279 on the ID threshold curve was not significant.

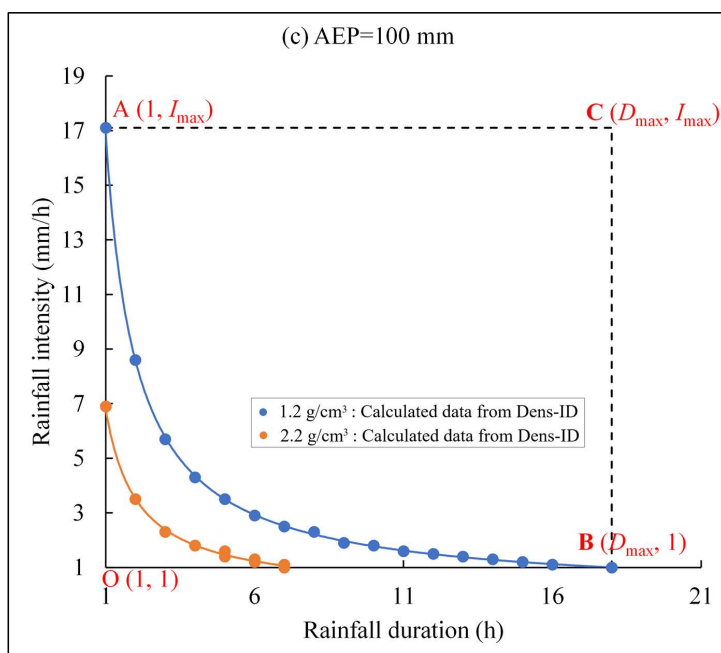


280



281





282

283 Fig.2 ID threshold curves derived by Dens-ID (the blue line corresponds to 1.2 g/cm<sup>3</sup>, and the  
 284 orange line corresponds to 2.2 g/cm<sup>3</sup> in the figures)

285 There are two ID threshold curves in each subplot of Fig. 2, which correspond to 1.2 g/cm<sup>3</sup> and  
 286 2.2 g/cm<sup>3</sup>, respectively. Because the debris flow density in JJG varies within a certain range from  
 287 1.2–2.3 g/cm<sup>3</sup>, the two ID threshold curves shown in each subplot can be regarded as the upper and  
 288 lower boundary lines for determining the occurrence of debris flow (Zhang et al., 2020). As shown  
 289 in Fig.2c, the two derived curves, together with the I- and D-axes, form a closed area in the ID  
 290 coordinate system; this area is denoted as  $W_{ID}$ . If the monitored rainfall, represented by the  
 291 combination of I and D, can enter  $W_{ID}$ , rainfall may trigger debris flows. As shown in each subplot,  
 292 the threshold curve can be represented by power function  $I=\alpha D^\beta$ . The variation intervals of the  
 293 independent (D) and dependent (I) variables of the power function are  $[1, D_{max}]$  and  $[1, I_{max}]$ ,  
 294 respectively, where  $D_{max}$  represents the rainfall duration required to trigger debris flow when  $I=1$

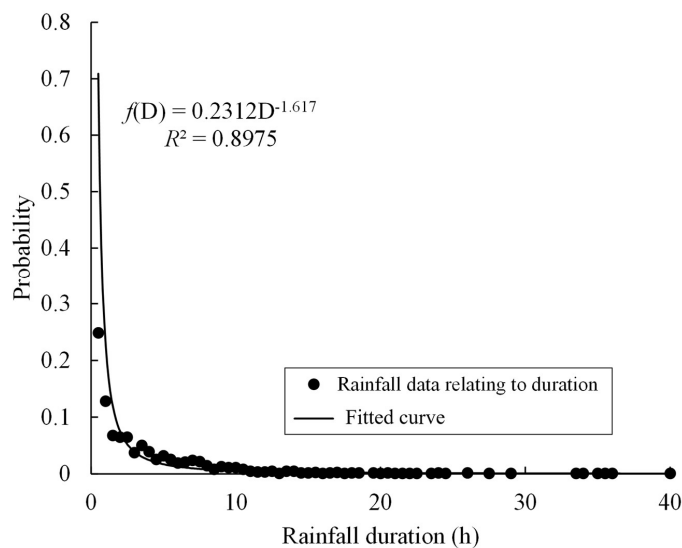




295 mm/h, and  $I_{\max}$  represents the rainfall intensity required for debris flow formation for  $D=1$  h. As  
296 shown in Fig.2c, independent variable  $D$  and dependent variable  $I$  can form a larger rectangular area  
297 (AOBC) in the  $ID$  plane than  $W_{ID}$ , which is denoted as  $R_{ID}$ . The coverage area of  $R_{ID}$  is much larger  
298 than that of  $W_{ID}$ , indicating that the proportion of rainfall conditions that can trigger debris flows is  
299 low. Therefore, even for  $AEP=100$  mm, the occurrence probability of debris flows remains low. As  
300 shown in each subplot, each  $AEP$  corresponds to a different  $W_{ID}$  and  $R_{ID}$ , which provides basic data  
301 for the quantitative evaluation of the effect of different  $AEP$ s on the occurrence probability of debris  
302 flows.

#### 303 4.2 Occurrence probability of debris flow under different AEP

304 Based on the Monte Carlo method of calculating the definite integral, it is necessary to explore  
305 the probability density function of rainfall duration ( $D$ ) to calculate the occurrence probability of  
306 debris flow under different  $AEP$  conditions. For the 1094 rainfall events listed in Appendix 1, we  
307 found that the probability distribution of rainfall duration  $D$  in JJG can be described by a power  
308 function (Fig. 3). As shown in Fig.3, the number of samples with  $D<1$  accounted for 37.7%,  $1<D<3$   
309 for 23.5%,  $3<D<5$  for 14.7%, and  $5<D<10$  for 16.9%; the number of rainfall events with  $D$   
310 exceeding 10 h accounted for only 6.7%.



311

312

Fig. 3 Probability density function of  $f(D)$

313 Based on the probability density distribution function  $f(D)=0.2312D^{-1.617}$ , the cumulative  
 314 probability function  $cdf(D)$  can be obtained through integration. In  $cdf(D)$ , denoted as Eq. 11, the  
 315 integration constant  $C$  needs to be determined.

316 
$$cdf(D) = \int_{-\infty}^D f(D) dD = -0.3747 * D^{-0.617} + C \quad (11)$$

317 The interval of 0–40 h was evenly divided into 56 statistical intervals (the second column in  
 318 Appendix 2, titled “appendix 2-f(D)and CFD(D).xlsx”), and each statistical interval was separated  
 319 by 0.5 h. The proportion of the sample size in each interval among the 1094 samples can be  
 320 calculated (second column in Appendix 2), and the cumulative proportion that increases with  $D$  is  
 321 obtained (third column in Appendix 2). The data in the first and third columns of Appendix 2 are  
 322 substituted into Eq. 11 to calculate  $C$ .  $C$  increases with  $D$  but gradually stabilizes at approximately  
 323 1.04 (the fifth column in Appendix 2), and  $C$  is set to 1.04.

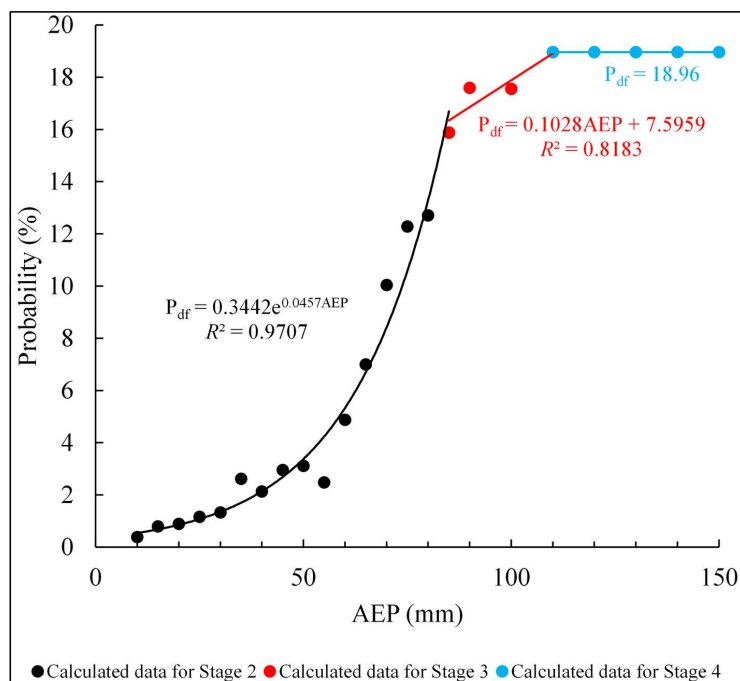
324 Based on the process of calculating  $P_{df}$  under different AEP conditions in Section 3.4, the  $P_{df}$   
 325 corresponding to each AEP in Table 1 was obtained, and the function  $P_{df} = f(AEP)$  for describing



326 their relationship was fitted using the AEP and  $P_{df}$  data.

$$327 \quad \begin{cases} P_{df} = 0 & 0 < AEP < 10 \\ P_{df} = 0.34e^{0.046AEP} & 10 \leq AEP < 85 \\ P_{df} = 0.1AEP + 7.6 & 85 \leq AEP < 110 \\ P_{df} = 18.96 & 110 \leq AEP \leq 130 \end{cases} \quad (12)$$

328 As shown in Eq.12,  $P_{df} = f(AEP)$  is a piecewise function. The evolution of  $P_{df}$  with AEP  
329 variation can be divided into four stages (Fig. 4). Two key issues must be stated before discussing  
330 these four stages in depth: (1) Based on the calculation results of the Dens-ID model, an upper limit  
331 volume of the rainfall-induced solid material supply is derived in JJG, which is the basic condition  
332 for determining the scale of debris flow in JJG (Zhang et al., 2020). (2) Based on the principle of  
333 water balance, AEP is defined as the rainfall that is preserved in the soil before the triggering rainfall  
334 process (Kohler and Linsley, 1951); field observations in JJG show that the AEP is positively  
335 correlated with the soil water content (Cui et al., 2007), and the field observations of the Liudaogou  
336 catchment in the northern Loess Plateau of China have the same result (Zhu and Shao, 2008);  
337 therefore, the AEP is typically used to estimate soil water content (Crozier, 1986; Chen et al., 2018;  
338 Zhao et al., 2019b). The water soil content before the triggering rainfall process can be characterized  
339 by AEP (Thomas et al., 2019; Schoener and Stone, 2020).



340

341 Fig.4 Relationship of  $P_{df}$  and AEP derived from Dens-ID (the black line represents the fitted curve  
342 of Stage 2, the red line represents the fitted curve of Stage 3, the blue line represents the fitted  
343 curve of Stage 4)

344 Stage 1: The probability of debris flow occurrence in JJG is equal to 0 when the AEP is < 10  
345 mm. Dens-ID estimates the solid material volume by simulating rainfall-induced shallow landslides.  
346 According to Eq. 4, the key hydrological process that triggers shallow landslides is the continuous  
347 increase in soil water content caused by rainfall infiltration. The increase in soil moisture content  
348 reduces soil matrix suction and eventually contributes to shallow landslides. The soil water content  
349 of the loose soil mass in JJG was low when the AEP was < 10 mm (Long et al., 2020), and a long  
350 duration of rainfall infiltration was needed to increase the soil water content. However, based on the  
351 infiltration border of Dens-ID (Eq. 1), limited by the infiltration capacity of the topsoil in JJG, the  
352 portion of precipitation that exceeds the infiltration capacity is converted into runoff; therefore,



353 when the water content of the soil layer in JJG is low, the surface runoff has already been generated.  
354 Accordingly, the runoff generation rate can be much higher than the supply rate of solid material in  
355 the Dens-ID simulation. In this hydrological scenario, Dens-ID determines that even a soil-water  
356 mixture with a density of  $1.2 \text{ g/cm}^3$  is difficult to generate in JJG; thus, the probability of debris  
357 flow is 0.

358 Stage 2: The relationship between  $P_{df} \sim AEP$  can be described by an exponential function,  
359 indicating that the probability of debris flow occurrence is enhanced by gradually increasing AEP.  
360 This trend obeys the following function:  $P_{df} = 0.3442e^{0.0457AEP}$ , which can be further divided into  
361 two subprocesses using  $AEP = 50 \text{ mm}$  as the demarcation point, where the slope of the curve  
362 changes significantly. Stage 2-1: When  $10 \text{ mm} \leq AEP \leq 50 \text{ mm}$ , the soil water content increased  
363 significantly compared to  $AEP < 10 \text{ mm}$ , but a necessary infiltration time to increase it to the critical  
364 state for triggering shallow landslides is still required. Therefore, limited by the supply rate of the  
365 solid material, the rate of increase of  $P_{df}$  was relatively low, and the maximum  $P_{df}$  was 3.11%. Stage  
366 2-2: When  $50 \text{ mm} < AEP \leq 85 \text{ mm}$ , the soil water content is relatively large compared to Stage 1; the  
367 solid material from shallow landslides can be immediately ready without a long rainfall infiltration  
368 duration, and a large soil water content of topsoil is beneficial to the rapid generation of runoff  
369 (Jones et al., 2017; Hirschberg et al., 2021). When there is a sufficient supply of provenance and  
370 runoff, the probability of debris flow occurrence in this subprocess is significantly enhanced by the  
371 increasing AEP.

372 Stage 3: After the AEP exceeded 85 mm, the rate of increase of  $P_{df}$  decreased, exhibiting a  
373 moderate linear increasing trend with AEP. Because of the very high soil water content, most of the  
374 loose soil layer in JJG is close to the saturated state (Long et al., 2020). Then, the total volume of



375 solid material reaches the maximum level, and the increased AEP can hardly contribute to the runoff  
376 generation rate. Consequently, the increasing trend of  $P_{df}$  slows compared with that in Stage 2-2.

377 Stage 4 ( $AEP \geq 110$  mm): According to the ID threshold curves in Table 1, the two key  
378 parameters  $\alpha$  and  $\beta$  of the threshold curve at this stage are already in a constant state, which means  
379 that there is no longer any change in  $R_{ID}$  and  $W_{ID}$  in Fig. 2c. Therefore, the  $P_{df}$  no longer changed  
380 with increasing AEP and remained unchanged at 18.96%.

#### 381 **4.3 Correlation analysis of the two curves derived from Dens-ID and observation data**

382 The AEP in Appendix 1 varied from 0–87.9 mm. Limited by this range, we can only test the  
383 reasonability of the first and second stages, as shown in Fig. 4. We introduce how to use the rainfall  
384 and debris flow data recorded in Appendix 1 to calculate  $P_{df}$ : (1) The original AEP value is rounded  
385 to one decimal place, and the rounded AEP are listed in the 8<sup>th</sup> column of Appendix 1, which were  
386 sorted from largest to smallest; (2) the maximum  $AEP_i$  was set to 90 mm, and  $[AEP_i, AEP_i-5]$  was  
387 used as the search window to collect the rainfall events and debris flow events; and (3) we count the  
388 number of debris flow events  $N_{df}$  and the number of rainfall events  $N_{rain}$  in each search window and  
389 then calculate  $P_{df} = N_{df}/N_{rain}$ . Based on the above steps, the collected data and calculated  $P_{df}$  are listed  
390 in Table 2. As shown in Table 2, a positive correlation between the probability of debris flow  
391 occurrence and AEP in JJG was determined. When  $AEP < 10$  mm, a total of 205 rainfall processes  
392 were recorded; however, no debris flow events were observed, and the debris flow occurrence  
393 probability was 0, which is consistent with the results of Stage 1 derived from Dens-ID.

394

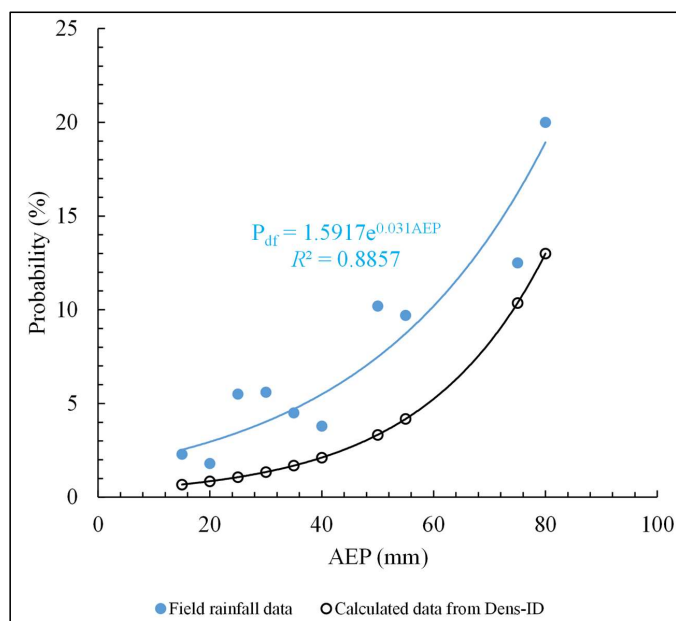
395



396 Table 2 Collected and calculated  $P_{df}$  in each search window

	Field observation data and calculated $P_{df}$										
AEP intervals	0-10	10-15	15-20	20-25	25-30	35-40	35-40	45-50	50-55	70-75	75-80
$N_{df}$	0	3	2	7	7	4	4	5	3	1	1
$N_{rain}$	205	133	111	127	124	106	106	49	31	8	5
$P_{df}$ (%)	0	2.3	1.8	5.5	5.6	3.8	3.8	10.2	9.7	12.5	20.0

397 Based on  $P_{df}$  and AEP listed in Table 2, their relationship can be described by the exponential  
 398 function denoted as  $P_{df} = 1.5917e^{0.031AEP}$ , which is similar to that of Stage 2 in Fig.4. Therefore,  
 399 two  $P_{df}$ -AEP curves derived from field observation data and the Dens-ID model were obtained for  
 400 further analysis, as shown in Fig.5. The two curves were nearly parallel. Eq. 12 is used to analyze  
 401 the correlation of the two curves, and  $r$  is equal to 0.93, suggesting they have a very high correlation.  
 402 Therefore, the function of  $P_{df} = f(AEP)$  derived from Dens-ID, which is used to describe the  
 403 evolution trend of debris flow occurrence probability with AEP variation, is reasonable.



404  
 405 Fig.5 Relationship of AEP and  $P_{df}$  obtained from field observation data and Dens-ID model (the blue line is



406 derived from field observation data, and the black line is derived from Dens-ID)

407 We can also see from Fig.5 that although the variation tendencies of the two curves are

408 consistent, there is a significant bias between them. As shown in Fig.5, the blue line fitted through

409 the observation data is above the black line derived from Dens-ID, indicating that Dens-ID

410 underestimated the probability of debris flow occurrence if the observation data were used as the

411 reference. However, we cannot conclude that there is a precision problem in the calculation results

412 of the Dens-ID. (1) Although 1094 rainfall processes and 37 debris flow events are field observation

413 data, there are many uncertain factors in Eq. 7 for calculating AEP using these rainfall data (Kim et

414 al., 2021), such as the subjectivity existing in  $K$  and  $n$  of Eq. 7, which render uncertainty in the

415 calculated AEP. In this case, if the data in Appendix 1 are used as the real value for evaluating the

416 precision of Dens-ID, the error evaluation result may be unfair to Dens-ID. In this case, it is unfair

417 to evaluate the Dens-ID error by using the calculated AEP in Appendix 1 as the true value. However,

418 this uncertainty can show consistent directional deviations because of the fixed values of  $K$  and  $n$  in

419 Eq.7; therefore, the uncertainty has no effect on the correlation analysis. (2) To establish the

420 functional relationship between  $P_{df}$ -AEP, a large number of rainfall scenarios were simulated using

421 the Dens-ID model. Dens-ID simulated 3376, 3182, 2677, and 2677 rainfall processes with AEP =

422 20, 40, 45, and 50 mm, respectively. The total number of simulated rainfall processes was

423 significantly larger than that of the 1094 observed rainfall events. The collected 1094 rainfall events

424 still cannot fully reflect all rainfall conditions in nature; that is, the amount of the observed 1094

425 rainfall data is still inadequate when used as the denominator for calculating the probability of debris

426 flow occurrence in JFG. Therefore, the  $P_{df}$  calculated using the field observation data may be

427 generally higher than that calculated using Dens-ID. (3) Dens-ID cannot fully and accurately





428 describe the formation process of the debris flow in JJG because of the simplification in theory and  
429 boundaries. Dens-ID is also affected by the accuracy of the input parameters (Zhang et al., 2020),  
430 which may eventually lead to deviations between the simulation results and field observations.

## 431 **5 Conclusions**

432 The Dens-ID model was used to derive the ID threshold curves corresponding to different AEP  
433 in the JJG. Thus, the Monte Carlo integral equation was used to construct the function of  $P_{df-AEP}$   
434 for a probability density distribution of field observation rainfall data. The functional relationship  
435 was verified using a large amount of field observation data from JJG. The following conclusions  
436 were drawn.

437 The qualitative conclusion recognized by scholars that "the greater the AEP, the higher the  
438 probability of subsequent rainfall triggering debris flow" is described by a clear mathematical  
439 equation in this study. For the probability of debris flow occurrence in JJG, the effective range of  
440 AEP that can affect debris flow formation was verified as 10–110 mm. Based on the simulation  
441 results, the probability of debris flow occurrence in JJG is 0 when  $AEP < 10$  mm, and the relationship  
442 between  $P_{df}$  and AEP can be described by an exponential function when  $10 \text{ mm} \leq AEP \leq 85$  mm.  
443 Limited by the total volume of provenance supply, infiltration capacity of topsoil, and soil saturation,  
444 when the AEP is greater than 85 mm, the growth rate of the probability curve slows, and the  
445 maximum  $P_{df}$  stabilizes at 18.96%. The plausibility of the first two evolution stages of the  $P_{df-AEP}$   
446 piecewise function is effectively confirmed by the field observation data because the  $P_{df-AEP}$   
447 relationship obtained from field observation data is highly correlated with the simulation results of  
448 Dens-ID. However, the reasonability of the last two stages of the  $P_{df-AEP}$  piecewise function cannot  
449 be tested because of the lack of field observation data, and the errors of the  $P_{df-AEP}$  piecewise



450 function cannot be verified because of the uncertainty of the AEP derived from the observation  
451 rainfall data.

452 This study mathematically confirms that "the greater the AEP, the higher the probability of  
453 subsequent rainfall triggering debris flow" and quantifies this qualitative conclusion using piecewise  
454 functions. This can effectively reveal the essential relationship between the two natural events of  
455 rainfall and debris flow, quantitatively describe the impact of different AEPs on the probability of  
456 debris flow occurrence, and provide key technical support for the early warning of debris flows.

#### 457 **Data availability**

458 No data sets were used in this article.

#### 459 **Author contributions**

460 All the authors searched, collected, and process the historical rainfall and debris flow data from JJG  
461 field observation station. Shaojie Zhang and Hongjuan Yang wrote parts of the paper, Both Shaojie  
462 Zhang and Kaiheng Hu are the Supervision and Funding acquisition, Juan Ma is responsible for  
463 Formal analysis, and Dunlong Liu is responsible for data curation.

#### 464 **Competing interests**

465 The contact author has declared that none of the authors has any competing interests.

#### 466 **Acknowledgement:**

467 This work was supported by the Chongqing Municipal Bureau of Land, Resources and Housing  
468 Administration (KJ-2021016), Project of the Department of Science and Technology of Sichuan  
469 Province (No. 2021YFG0258), National Natural Science Foundation of China (No. 42001100).

#### 470 **References**

471 Abraham, M.T., Satyan, N., Rosi, A., Pradhan, B., Segoni, S.: Usage of antecedent soil moisture for



- 472 improving the performance of rainfall thresholds for landslide early warning. *Catena*, 200,  
473 105147, 2021.
- 474 Abraham, M.T., Satyam, N., Pradhan, B., Alamri, A.M.: Forecasting of landslides using rainfall  
475 severity and soil wetness: A probabilistic approach for Darjeeling Himalayas. *Water (Switzerland)*  
476 12, 1–19, 2020.
- 477 Adams, B., Fraser, H., Howard, C., Hanafy, M.: Meteorological data analysis for drainage system  
478 design. *J. Environ. Eng.* 112, 1986.
- 479 Albert, G.E.: A general theory of stochastic estimates of the Neumann series for solution of certain  
480 Fredholm integral equations and related series, in: M.A. Meyer (Ed.), *Symposium of Monte Carlo*  
481 *Methods*, Wiley, New York, 1956.
- 482 Bel, C., Liébault, F., Navratil O., Eckert N., Bellot H., Fontaine, F., Laigle, D.: Rainfall control of  
483 debris-flow triggering in the Réal Torrent, Southern French Prealps, 291, 17-32, 2017.
- 484 Bennett, G.L., Molnar, P., Mcardell, B.W., Burlando, P.: A probabilistic sediment cascade model of  
485 sediment transfer in the Illgraben. *Water Resources Research*, 50, 1225-1244, 2014.
- 486 Bernard, M., Gregoretti, C.: The use of rain gauge measurements and radar data for the model-based  
487 prediction of runoff-generated debris flow occurrence in early warning systems. *Water Resources*  
488 *Research*, 57, e2020WR027893, 2021.
- 489 Berti, M., Simoni, A.: Experimental evidences and numerical modelling of debris flow initiated by  
490 channel runoff. *Landslides*, 3, 171-182, 2005.
- 491 Calvo, B., Savi, F.: A real-world application of Monte Carlo procedure for debris flow risk  
492 assessment, *Computers and Geosciences*, 35(5), 967-977, 2009.
- 493 Castillo, V.M., Gómez-Plaza, A., Martínez-Mena, M.: The role of antecedent soil water content in



- 494 the runoff response of semiarid catchments: a simulation approach. *Journal of Hydrology*, 284,  
495 114-130, 2003.
- 496 Chen, C.W., Oguchi, T., Chen, H., Lin, G.W. Estimation of the antecedent rainfall period for mass  
497 movements in Taiwan, *Environmental Earth Sciences*, 77, 184, 2018.
- 498 Chen, C.W., Saito, H., Oguchi, T.: Analyzing rainfall-induced mass movements in Taiwan using the  
499 soil water index, *Landslides*, 14, 1031-1041, 2017.
- 500 Coe, J.A., Kinner, D.A., Godt, J.W. Initiation conditions for debris flows generated by runoff at  
501 Chalk Cliffs, central Colorado. *Geomorphology*, 3, 270-297, 2008.
- 502 Crozier, M.J.: *Landslides: causes, consequences & environment*. Croom Helm, London, p 25, 1986.
- 503 Cui, P., Zhu, Y.Y., Chen, J., Han, Y.S., Liu, H.J.: Relationships between antecedent rainfall and  
504 debris flows in Jiangjia Ravine, China. In: Chen & Major, eds., *Debris-Flow Hazards Mitigation:*  
505 *Mechanics, Prediction, and Assessment*, Millpress, Netherlands, 3-10, 2007.
- 506 De Vita, P.: Fenomeni d'instabilita` delle coperture piroclastiche dei Monti Lattari, di Samo e di  
507 Salerno (Campania) ed analisi degli eventi pluviometrici determinanti. *Quad. Geol. Appl.*, 7, 213–  
508 239, 2000.
- 509 Donovan, I.P., Santi, P.M. A probabilistic approach to post-wildfire debris-flow volume modeling,  
510 *Landslides*, 14(4): 1345-1360, 2017.
- 511 Fiorillo, F., Wilson, R.C. Rainfall induced debris flows in pyroclastic deposits, Campania (southern  
512 Italy). *Engineering Geology*, 75, 263-289, 2004.
- 513 Gabet, E.J., Mudd, S.M.: The mobilization of debris flows from shallow landslides. *Geomorphology*  
514 1, 207-218, 2006.
- 515 Han, Z., Chen, G.Q., Li, Y.G., He, Y.: Assessing entrainment of bed material in a debris-flow event:



516 a theoretical approach incorporating Monte Carlo method: Assessing Entrainment of Bed  
517 Material by Debris Flow, *Earth surface processes and landforms*, 40(14): 1877-1890, 2015.

518 Hirschberg, J., Badoux, A., McArdell, B.W., Leonarduzzi, E., Molnar, P.: Evaluating methods for  
519 debris-flow prediction based on rainfall in an Alpine catchment. *Nat. Hazards Earth Syst. Sci.*,  
520 21, 2773-2789, 2021.

521 Hong, M., Kim, J., Jeong, S.: Rainfall intensity-duration thresholds for landslide prediction in South  
522 Korea by considering the effects of antecedent rainfall. *Landslides*, 15, 523–534, 2018.

523 Hu, W., Xu, Q., Wang, G.H., van Asch, T.W.J., Hicher, P.Y.: Sensitivity of the initiation of debris  
524 flow to initial soil moisture. *Landslides* 12, 1139–1145, 2015.

525 Huang, C.H.: Critical rainfall for typhoon-induced debris flows in the Western Foothills, Taiwan.  
526 *Geomorphology*, 185, 87-95, 2013.

527 Hürlimann, M. Coviello, V., Bel, C., Guo, X.J., Berti, M., Graf, C., Hübl, J., Miyata, S., Smith, J.B.,  
528 Yin, H.Y.: Debris-flow monitoring and warning, Review and examples. *Earth-Science Reviews*,  
529 199, 102981, 2019.

530 Iverson, R. M., Reid, M. E., LaHusen, R. G.: Debris Flow Mobilization from Landslides. *Annu. Rev.*  
531 *Earth Planet*, 25: 85-138, 1997.

532 Jones, R., Thomas, R.E., Peakall, J., Manville, V.: Rainfall-runoff properties of tephra: Simulated  
533 effects of grain-size and antecedent rainfall. *Geomorphology*, 282, 39-51, 2017.

534 Kim, S.W., Chun, K.W., Kim, M., Catani, F., Choi, B., Seo, J.: Effect of antecedent rainfall  
535 conditions and their variations on shallow landslide-triggering rainfall thresholds in South Korea.  
536 *Landslides*, 18, 569-582, 2021.

537 Kohler, M.A., Linsley, R.K.: Predicting the runoff from Storm Rainfall. US Department of



- 538 Commerce, Weather Bureau, Washington, D.C., 1951.
- 539 Le Bissonnais, Y., Renaux, B., Delouche, H. Interactions between soil properties and moisture  
540 content in crust formation, runoff and interrill erosion from tilled loess soils. *Catena*, 25(1), 33-  
541 46, 1995.
- 542 Li, L., Zhang, S.X., Li, S.H., Qiang, Y., Zheng, Z., Zhao, D.S.: Debris Flow Risk Assessment  
543 Method Based on Combination Weight of Probability Analysis, *Advances in civil engineering*,  
544 2021, 1-12, 2021.
- 545 Liu, D.L., Zhang, S.J., Yang, H.J., Zhao, L.Q., Jiang, Y.H., Tang, D., Leng, X.P.: Application and  
546 analysis of debris-flow early warning system in Wenchuan earthquake-affected area. *Nat. Hazards*  
547 *Earth Syst. Sci.*, 16, 483-496, 2016.
- 548 Liu, X.L., Wang, F., Nawnit, K., Lv, X.F., Wang, S.J. Experimental study on debris flow initiation.  
549 *Bulletin of Engineering Geology and the Environment*, 79, 1565-1580, 2020.
- 550 Long, K., Zhang, S.J., Wei, F.Q., Hu, K.H., Zhang, Q., Luo, Y. A hydrology-process based method  
551 for correlating debris flow density to rainfall parameter and its application on debris flow  
552 prediction. *Journal of Hydrology*, 589, 125124, 2020.
- 553 Luk, S.H.: Effect of antecedent soil moisture content on rainwash erosion. *Catena*, 12, 129-139,  
554 1985.
- 555 Marra, F., Destro, E., Nikolopoulos, E.I., Zoccatelli, D., Creutin, J.D., Guzzetti, F., Borga, M.:  
556 Impact of rainfall spatial aggregation on the identification of debris flow occurrence thresholds.  
557 *Hydrol. Earth Syst. Sci.*, 21, 4525-4532, 2017.
- 558 Paola, F.De., Risi, R.De., Crescenzo, G. Di, Giugni, M., Santo, A., Speranza, G.: Probabilistic  
559 Assessment of Debris Flow Peak Discharge by Monte Carlo Simulation, *Journal of Risk and*



- 560 Uncertainty in Engineering Systems, Part A: Civil Engineering, 3(1), A4015002, 2017.
- 561 Papa, M.N., Medina, V., Ciervo, F., Bateman, A.: Derivation of critical rainfall thresholds for  
562 shallow landslides as a tool for debris flow early warning systems. *Hydrol. Earth Syst. Sci.* 17,  
563 4095-4107, 2013.
- 564 Peres, D.J., Cancelliere, A.: Derivation and evaluation of landslide-triggering thresholds by a Monte  
565 Carlo approach. *Hydrol. Earth Syst. Sci.*, 18, 4913-4931, 2014.
- 566 Peres, D.J., Cancelliere, A.: Modeling impacts of climate change on return period of landslide  
567 triggering. *Journal of Hydrology*, 567, 420-434, 2018.
- 568 Richards, L.A. Capillary condition of liquids in porous mediums. *Physics* 1, 318-333, 1931.
- 569 Schoener, G., Stone, M.C.: Monitoring soil moisture at the catchment scale-A novel approach  
570 combining antecedent precipitation index and radar-derived rainfall data, *Journal of Hydrology*,  
571 589, 125155, 2020.
- 572 Segoni, S., Piciullo, L., Gariano, S.L.: A review of the recent literature on rainfall thresholds for  
573 landslide occurrence, *Landslides*, 15:1483-1501, 2018b.
- 574 Segoni, S., Rosi, A., Lagomarsino, D., Fanti, R., Casagli, N.: Brief communication: Using averaged  
575 soil moisture estimates to improve the performances of a regionalscale landslide early warning  
576 system. *Nat. Hazards Earth Syst. Sci.* 18, 807-812, 2018a.
- 577 Senthilkumar, V., Chandrasekaran, S.S., Maji, V.B.: Geotechnical characterization and analysis of  
578 rainfall-induced 2009 landslide at Marappalam area of Nilgiris district, Tamil Nadu state, India.  
579 *Landslides*, 14, 1803-1814, 2017.
- 580 Tang, H., Mcguire, L.A., Kean, J.W., Smith, J.B.: The impact of sediment supply on the initiation  
581 and magnitude of runoff-generated debris flows. *Geophysical Research Letters*, 47,



- 582 e2020GL087643, 2020.
- 583 Thomas, M.A., Collins, B.D., Mirus, B.B.: Assessing the feasibility of satellite-based thresholds for  
584 hydrologically driven landsliding. *Water Resource Research*, 55, 9006-9023, 2019.
- 585 Tisdall, A.: Antecedent soil moisture and its relation to infiltration. *Aust. J. Agric. Res.*, 2 (3), 342–  
586 348, 1951.
- 587 Van Genuchten, M.: A closed form equation for predicting the hydraulic conductivity of unsaturated  
588 soils. *Soil Sci. Soc. Am. J.* 44, 892–898, 1980.
- 589 Wei, F.Q., Hu, K.H., Zhang, J., Jiang, Y.H., Chen, J.: Determination of effective antecedent rainfall  
590 for debris flow forecast based on soil moisture content observation in Jiangjia Gully, China. In:  
591 DeWraichien, D., Brebbia, C.A., Lenzi, M.A., eds., *Monitoring, Simulation, Prevention and*  
592 *Remediation of dense debris flows II*. WIT Transactions on Engineering Sciences, England. 13-  
593 22, 2008.
- 594 Yan, Z.Z., Hong, Z.M.: Using the Monte Carlo method to solve integral equations using a modified  
595 control variate. *Applied mathematics and computation*, 242,764-777, 2014.
- 596 Yang, H.J., Zhang, S.J., Hu, K.H., Wei, F.Q., Wang, K., Liu S.: Field observation of debris flow  
597 activities in the initiation area of Jiangjia Gully, Yunnan Province, China, *Journal of Mountain*  
598 *Science*, 19(6): 1602-1617, 2022.
- 599 Zhang, S.J., Xu, C.X., Wei, F.Q., Hu, K.H., Xu, H., Zhao, L.Q., Zhang, G.P.: A physics-based model  
600 to derive rainfall intensity-duration threshold for debris flow. *Geomorphology*, 351, 106930, 2020.
- 601 Zhang, S.J., Yang, H.J., Wei, F.Q., Jiang, Y.H., Liu, D.L.: A model of debris flow forecast based on  
602 the water-soil coupling mechanism. *Journal of Mountain Science*, 25, 757-763, 2014.
- 603 Zhao, B.R., Dai, Q., Han, D.W., Dai, H.C., Mao, J.Q., Zhuo, L.: Probabilistic thresholds for





604      landslides warning by integrating soil moisture conditions with rainfall thresholds, *Journal of*  
605      *Hydrology*, 574, 276-287, 2019a.

606      Zhao, B.R., Dai, Q., Han, D., Dai, H., Mao, J., Zhuo, L., Rong, G.: Estimation of soil moisture using  
607      modified antecedent precipitation index with application in landslide predictions. *Landslides* 16,  
608      2381–2393, 2019b.

609      Zhu, Y.J., Shao, M.G.: Variability and pattern of surface moisture on a small-scale hillslope in  
610      Liudaogou catchment on the northern Loess Plateau of China, *Geoderma*, 147, 185-191, 2008.

611      Zhuang, J.Q., Cui, P., Wang, G.H., Chen, X.Q., Iqbal, J., Guo, X.J.: Rainfall thresholds for the  
612      occurrence of debris flows in Jiangjia Gully, Yunnan Province, China. *Eng. Geol.* 195, 335–346,  
613      2015.